AAPS PharmSciTech, Vol. 14, No. 3, September 2013 (© 2013)
DOI: 10.1208/s12249-013-9980-y

Research Article

Cubic Magnetically Guided Nanoaggregates for Inhalable Drug Delivery: *In Vitro* Magnetic Aerosol Deposition Study

Doaa Mohamed Ragab[1,2,3] and Sohrab Rohani[1]

Received 24 January 2013; accepted 8 May 2013; published online 14 June 2013

Abstract. The present work describes the *in vitro* aerosol deposition and enhanced deaggregation behavior of superparamagnetic iron oxide nanoaggregates (SPIONs). SPIONs were surface-coated with amine functionalized polyrotaxane and were proposed as a carrier for inhalation dry powders. Polyrotaxane is primarily composed of beta cyclodextrin rings which are spontaneously threaded on the block copolymer, poly(propylene glycol) bis(2-aminopropylether). Variable concentrations of surface coating polymers showed controlled manipulation of the crystal size and morphology. Magnetic nanoaggregates fabricated with low concentration of polyrotaxane showed cubic crystal morphology. However, these nanoaggregates exhibited rhombic dodecahedron crystal structure upon increasing the coating polymer concentration. In comparison to the spherical uncoated magnetic nanoparticles, cubic phase magnetic nanoaggregates demonstrated an enhanced *in vitro* aerosol deposition using magnetic field alignment. This enhancement can be accomplished at low inhalation flow rates (15 and 30 L/min). However, transformation to the cubic crystal structure was observed to be associated with a reduction in the powder geometric standard deviation. Using a mathematical modeling approach, we noted significant enhancement in the deaggregation behavior of inhalation dry powders; that can be achieved with small amounts of magnetic nanoaggregates. Aggregates of cubic nanoparticles showed promise for targeted pulmonary deposition of anticancer drugs.

KEY WORDS: *in vitro* aerosol deposition; magnetic nanoaggregates; magnetic next generation impinger; polyrotaxane; saturation magnetization.

INTRODUCTION

Polymeric nanoparticles have been successfully applied for pulmonary delivery of both local and systemic drugs (1). The respiratory route is particularly advantageous due to the large alveolar surface area, the low thickness of the epithelial barrier as well as the extensive vascular properties (2). With the recent development of nanotechnology, aerosols composed of magnetic nanoparticles showed several attractive properties for application in respiratory drug delivery (3,4). Magnetic nanoparticles have been applied in wastewater treatment (5). Presently, magnetic nanoparticles have gained increasing attention in biomedical applications such as magnetic resonance imaging (5–7), virus detection (8,9), magnetic cell separation (10), gene therapy (11), targeting chemotherapy (12), and pulmonary drug delivery (3,6).

A major challenge in pulmonary drug delivery is the low efficiency of the inhalation system. Optimum particle size is very important for deep lung delivery (13). Therefore, large doses of drugs need to be administered to achieve the effective drug concentration at the specific site of action. Current efforts are focused on developing magnetic nanoparticles that can be directed to a specific location of the pulmonary tract. These nanoparticles are responsive to an external thermal stimulus, i.e., the heating effect associated by alternating an external magnetic field (14). Given the limited knowledge of selective cancer biomarkers, specific cell targeting can be managed through conjugation of magnetic nanoparticles with a specific ligand (4,15,16).

Magnetic nanoparticles need to be stable in water at neutral pH (7.4) and normal saline condition (150 mmol) for biological, medical diagnostic, and therapeutic applications. Thus, the surface of magnetic iron oxide cores needs to be modified to prevent the formation of large aggregates and provide functional groups (amine or carboxylic groups) for bio-conjugation to anti-cancer drugs and/or targeted ligands. Various surface coatings have been reported previously, such as liposomes (17,18), polyethylene glycol (PEG) (19), and other polymers (20). In case of the surface coating with another material, this technique leads to the formation of "hybrid nanostructure" (21). Magnetic nanoparticles coated with PEGs and beta cyclodextrin have been reported to improve the drug loading and release kinetics of hydrophobic drugs

Electronic supplementary material The online version of this article (doi:10.1208/s12249-013-9980-y) contains supplementary material, which is available to authorized users.

[1] Department of Chemical and Biochemical Engineering, University of Western Ontario, 1151 Richmond Street, London, Ontario, Canada N6A 3K7.
[2] Department of Industrial Pharmacy, Alexandria University, Alexandria, Egypt.
[3] To whom correspondence should be addressed. (e-mail: ddoaamoh@uwo.ca)

(22), increase the specific cancer targeting, and enhance permeability and retention effects (23,24).

Harada and coworkers have reported the complex formation between polypropylene glycol and beta cyclodextrin (25). The proposed structure for these complexes is that the beta cyclodextrin rings are spontaneously threaded onto polypropylene glycol chains in either a head-to-head or tail-to-tail arrangements without any covalent bonding between the two polymers (beta cyclodextrin and polypropylene glycol). In the current study, we proposed a modified method for the synthesis of amine functionalized polyrotaxane through the formation of beta cyclodextrin/poly(propylene glycol) bis(2-aminopropylether) inclusion complex. Introducing an amino-functional group into the structure of polyrotaxane leads to the formation of highly functional and biocompatible hybrid nanostructures. These magnetic nanostructures possess an enhanced localization of anti-cancer loaded nanoparticles into the lung cancer cells. Therefore, they are promising materials for use in treatment of lung cancer (26).

The present study deals with amine functionalized polyrotaxane/iron oxide hybrid aggregates for pulmonary drug delivery. These hybrid nanostructures composed of magnetic iron oxide cores and polyrotaxane (PR) shells (Fe_3O_4 aggregates/PR). Magnetic nanoparticles coated with polyethylene block copolymers possess the ability to circulate for longer time in the blood stream by avoiding the uptake by the reticuloendothelial system (27,28). The influence of magnetic field on the systemic absorption and clearance of magnetic nanoparticles was previously reported (29,30). The magnetic field application resulted in considerable enrichment of therapeutic agent in the lungs and a depletion in the liver of the magnetic carrier compared to a reference without a magnetic field (29).

However, the application of external magnetic field did not change the accumulation of magnetic nanoparticles in the lung following their intravenous injection. Therefore, pulmonary delivery of magnetic nanoparticles showed a promise for an enhanced therapeutic effectiveness (30).

In the current research, we investigated the *in vitro* aerosol deposition of magnetic aggregates loaded for the potential aerosol delivery of anticancer drugs. The aerosol deposition was assessed with the application of an external magnetic field. The influence of variable concentration of poly(propylene glycol) bis(2-aminopropylether) (PPG-NH2) showed significant effect on the particle shape. In addition, we investigated the aerosolization behavior of magnetic aggregates exposed to an external magnetic field with field strength of 1 T. This study was conducted using a modified next generation magnetic setup. To the best of our knowledge, there is no previous study dealing with the utilization of magnetic next generation impinger (mNGI) in measurement of the aerodynamic diameter. However, a previous study was conducted on the *in vitro* deposition of magnetic particles in a simulated lung model (31).

MATERIALS AND METHODS

Materials

The following materials were used: $FeSO_4.7H_2O$ (VWR, Mississauga, ON, Canada), poly(propylene glycol) bis(2-aminopropylether) [average molecular weight, M_n, 230, Sigma-Aldrich Ltd, Oakville, ON, Canada), beta cyclodextrin (molecular weight 1,135 Da, Sigma-Aldrich Ltd, Oakville, ON, Canada), tetrahydrofuran (Sigma-Aldrich Ltd, Oakville, ON, Canada), and ethanol and ammonium hydroxide (VWR, Mississauga, ON, Canada).

Synthesis of Magnetic Nanoparticles

Spherical Magnetic Nanoparticles (Fe_3O_4). Spherical magnetic nanoparticles were prepared by chemical precipitation of (ferrous sulfate heptahydrate, $FeSO_4.7H_2O$) (22,32). The prepared nanoparticles showed a relatively wider size distribution than the polymer-coated formulae (polydispersity index=0.39). Results for the polydispersity indices are presented in Table I.

PPG-NH2-Coated Magnetic Nanoparticles. PPG-NH2 surface-modified magnetic nanoparticles were prepared by mixing a predetermined amount of iron precursor with the amine functionalized poly(propylene glycol) block copolymer (PPG-NH2).

Synthesis of Amine Functionalized Polyrotaxane. The synthesis of polyrotaxane inclusion complex was previously reported by Harada *et al.* (25). The modification we introduced to the synthesis was the inclusion of amine functionalized poly(propylene glycol) block copolymer into the cavity of beta cyclodextrin. The detailed synthetic method and the molar ratios of both polymers are provided in the supplementary section. The chemical structure of the prepared inclusion complex is presented in Scheme 1.

Table I. Influence of PPG-NH2, Poly(propylene glycol) bis(2-Aminopropylether), Concentration on the Estimated TEM and XRD Particles' Diameters, and on the MMAD (Measured by the Magnetic Next Generation Impinger)

PPG-NH2 concentration (mg/100 mg nanoparticles)	TEM particle diameter (nm±RSD)	Polydispersity index	XRD particle diameter (nm)	Nanoaggregates MMAD at 60 L/min (μm±GSD)
0	92.54±10.11	0.39	106.48	3.52±1.80
50	75.50±7.55	0.29	63.74	3.37±1.48
100	60.60±7.58	0.12	55.66	2.97±1.41
150	53.30±7.19	0.24	52.25	2.44±1.53
200	26.50±3.71	0.19	26.28	2.06±1.32
250	18.70±2.06	0.14	23.90	1.89±1.25
300	17.79±2.31	0.08	17.99	1.79±1.20

PPG-NH2 poly(propylene glycol) bis(2-aminopropylether), *TEM* transmission electron microscope, *RSD* relative standard deviation, *XRD* X-ray diffraction, *MMAD* mass median aerodynamic diameter, *GSD* geometric standard deviation

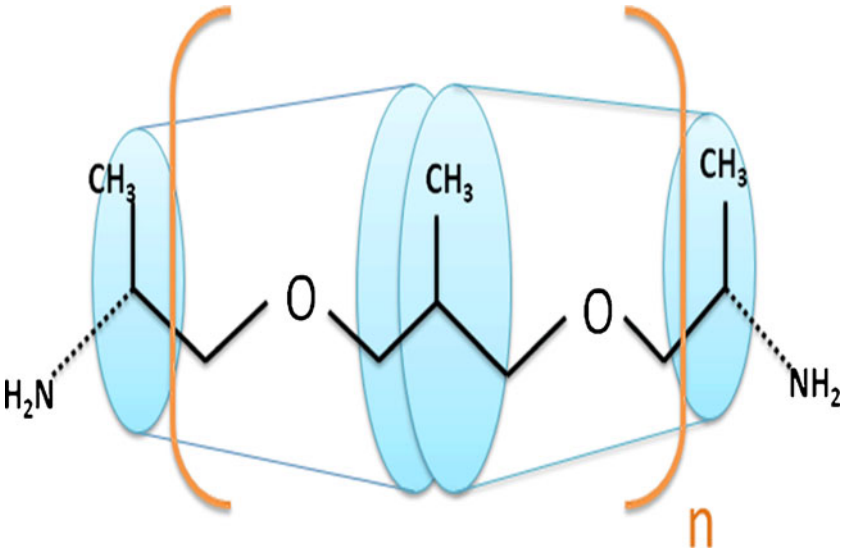

Scheme 1. Chemical structure polyrotaxane inclusion complex showing two beta-cyclodextrin molecules threaded onto poly(propylene glycol) bis(2-aminopropylether). This scheme is based on the structure proposed in (25)

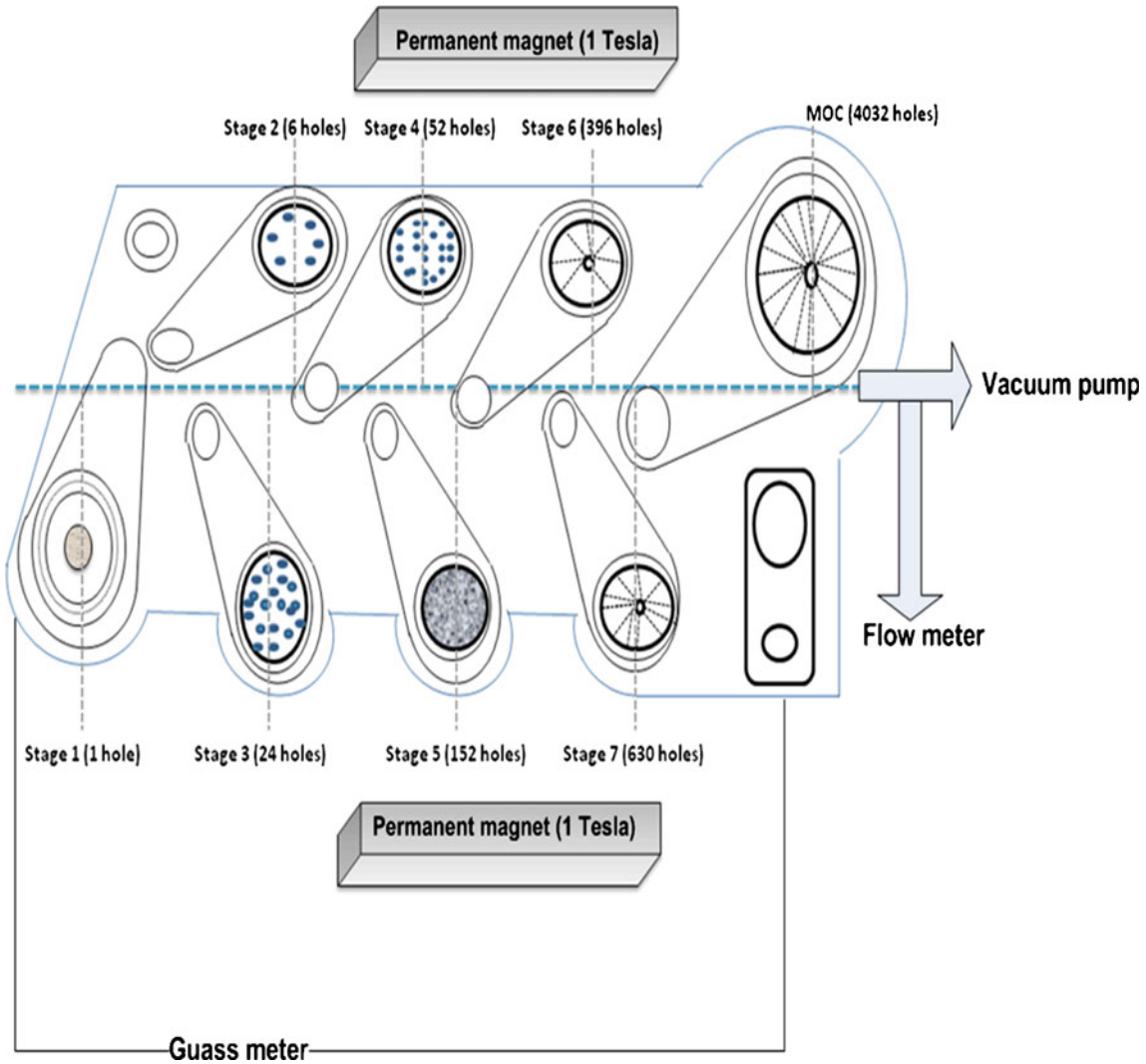

Scheme 2. Schematic diagram of magnetic next generation impinger setup

Polyrotaxane-Coated Magnetic Nanoparticles. In these samples, the amounts of amine functionalized polyrotaxane were varied from 50 to 300 mg/100 mg of nanoparticles. Increasing the inclusion complex concentration resulted in morphological transformation of magnetic nanoparticles from cubic to rhombic dodecahedron crystals.

Characterization of Magnetic Aggregates

Particle Size and Morphology. Magnetic nanoparticles size and morphology were evaluated using transmission electron microscope (TEM) (Hitachi High-Technologies GmbH, Krefeld, Germany). The morphology of particles was also examined using scanning electron microscopy, with a scanning electron 600F model microscope (Jeol Ltd, Tokyo, Japan). The samples were prepared on aluminum stabs and coated with gold prior to the examination.

X-ray Diffraction. X-ray diffractometer (Rigaku-Miniflex, The Woodlands, TX, USA) was utilized for examination of the crystal profile of loaded and unloaded samples. The samples were exposed to X-ray radiation (Cu K α, 40 KV, 20 mA) at a wavelength of 1.54 Å. The samples were scanned over a 2-theta range between 15° to 70° and at a step size of 0.02°.

Fourier Transform Infrared Spectroscopy. Fourier transform infrared spectroscopy (FTIR) spectra were in the solid state by Bruker-Vector 22 FTIR spectrophotometer (Bruker-Vector, Milton, ON, Canada).

Thermo-gravimetric Analysis. Magnetic aggregates samples were examined using thermogravimetric analysis (TGA)-SDTA 851 instrument (Mettler Toledo, Mississauga, ON, Canada). Samples (10 mg) were heated from 25°C to 600°C at a rate of 20°C/min under continuous purge of nitrogen gas.

Dynamic Light Scattering. Malvern dynamic light scattering (Malvern Instruments Ltd., Worcestershire, UK) was utilized to examine the size of synthesized polymer-coated magnetic aggregates. The polydispersity index as well as the mean volume diameter was examined. The obtained data represent the volume median diameters of nanoparticles. The corresponding aerodynamic diameter was theoretically calculated as follows:

$$D_{\text{aer}} = \sqrt{\frac{\rho}{\rho_1}}\text{VMD} \qquad (1)$$

where ρ is the tap density and ρ_1=1 g/cm^3 (33). The powder density was measured using a TAP-2S tap density tester (Logan Instruments CORP, Somerset, NJ, USA).

In Vitro Magnetic Aerosol Deposition

The purpose of these experiments was to investigate the *in vitro* aerosol deposition of magnetic nanoparticles using a mNGI setup (Scheme 2). The construction of the mNGI was modified based on the design outlined for the next generation impinger in previous publications (34,35). For each magnetic aggregates sample, the flow rate throughout the mNGI was varied between 15 and 100 L/min by the utilization of a calibrated flow meter (TSI 3063, TSI instruments Ltd., Buckinghamshire, UK). The magnetic field values were measured as a function of the calculated upper cut-off diameter on each stage of mNGI and at variable flow rates. The cut-off diameters for the mNGI at different inhalation flow rates are listed in Table S-1 (Supplementary section). The magnetic dry powders are delivered through a Handihaler® (Boehringer Ingelheim Inc., Ridgefield, CT, USA).

A preliminary experiment was conducted on a standard lactose sample (mass median aerodynamic diameter (MMAD)=5 μm, geometric standard deviation (GSD)=1.82) in order to evaluate the cut-off diameters for NGI and mNGI. The data examined for both impingers indicate similarity in MMAD and GSD for both impingers, which suggests that the modifications made to the NGI have not significantly affected its particle sizing capabilities. All modifications done to the NGI are the application of an external magnetic field, which has no effect on the function of the collection cups.

The cumulative mass of particles deposited on each stage of mNGI was calculated and plotted as percentage of the total mass of powder exiting the inhaler device. The MMAD and the GSD were calculated for each sample based on the previously reported expressions (33).

Magnetic Field and Powder Magnetization

The magnetic field at each stage of mNGI was measured by a Gaussmeter (5180 Gaussmeter, Pacific-Scientific-OECO, Milwaukie, OR, USA), and the powder magnetization values were measured using vibrating sample magnetometer (Model 74035, Lake Shore Cryotronics Inc., Westerville, OH, USA) at 300 K. The magnetic properties of aggregates samples were studied at field range of ±10,000 gauss.

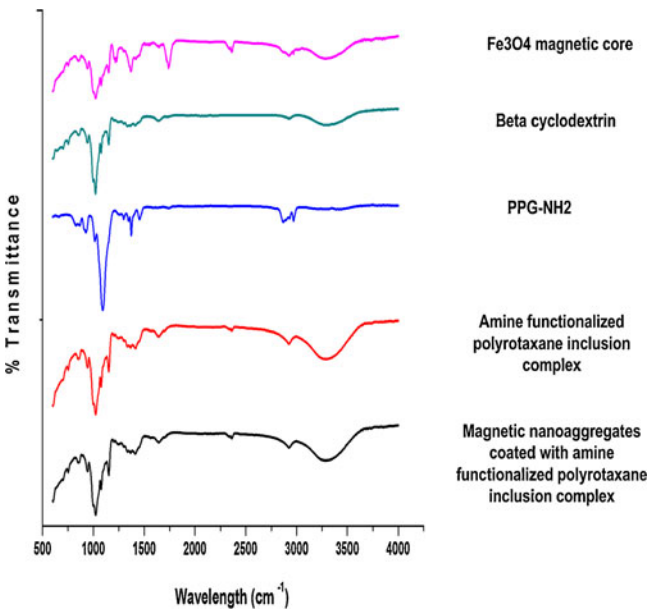

Fig. 1. FTIR spectra of uncoated magnetic core, beta-cyclodextrin, poly(propylene glycol) bis(2-aminopropylether) "PPG-NH2," polyrotaxane inclusion complex, and polyrotaxane-coated magnetic aggregates

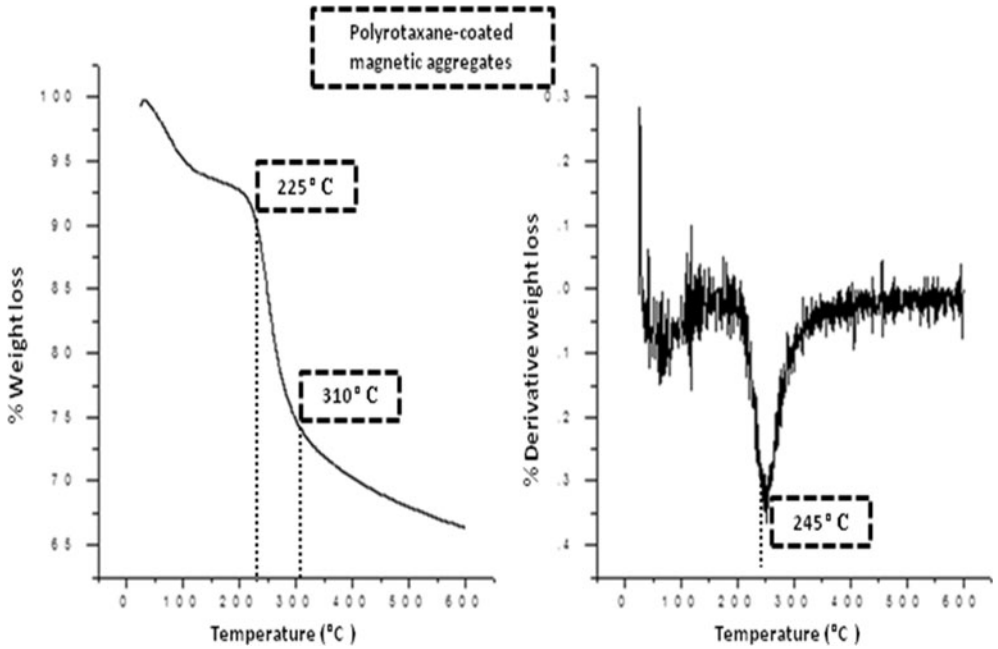

Fig. 2. TGA profile of polyrotaxane-coated magnetic aggregates and its first derivative plot

Mathematical Modeling of Powder Dispersion Behavior

For further monitoring of the extent of powder dispersion upon exposure to an increasing air flow rate, a deaggregation index was introduced. The deaggregation index was calculated by dividing the theoretically calculated D_{aer} by the experimentally measured MMAD (33). The change in the calculated deaggregation index as a function of the air flow rate was monitored. This experiment was continued till complete powder dispersion was achieved, which can be confirmed by a plateau in the de-aggregation index-air flow rate profiles. In order to compare the dispersion behavior of different magnetic samples, the calculated de-aggregation index-air flow rate profiles were mathematically fitted to the following three-parameter sigmoid equation:

$$\text{Deaggregation index} = \frac{D_{aer}}{\text{MMAD}} = \frac{a}{1 + e^{\frac{(x-x_0)}{b}}} \qquad (2)$$

where parameter (a) is the maximum de-aggregation index that can be achieved upon increasing the air flow rate to 100 L/min and (x_0) is the minimum air flow rate required to produce a de-aggregation index value equals to 0.5. The rate of dispersion process is presented by parameter (b), which is the difference between the two air flow rates required to achieve a de-aggregation index values equals to 0.75 and 0.25 (36). In other words, the curve fitting parameters (a) and (b) represent the extent and rate of dispersion process, respectively.

RESULTS

Characterization of Aggregates

TGA, DTGA, and FTIR. In this paper, we examined the effect of using PPG-NH2 or polyrotaxane on the morphological and crystal structure of magnetic nanoparticles. Recently, we reported the capability of these magnetic

Table II. Effect of Polyrotaxane Concentration and Air Flow Rate on the Calculated Mass Median Aerodynamic Diameter of Magnetic Aggregates

Polyrotaxane concentration (mg/100 mg nanoparticles)	Nanoaggregates MMAD (μm±GSD) 15 (L/min)	Nanoaggregates MMAD (μm±GSD) 30 (L/min)	Nanoaggregates MMAD (μm±GSD) 60 (L/min)	Nanoaggregates MMAD (μm±GSD) 100 (L/min)
0	1.79±1.20	1.15±1.24	0.78±1.26	0.59±1.29
50	1.51±1.31	0.94±1.37	0.63±1.41	0.46±1.45
100	1.35±1.11	0.82±1.14	0.55±1.16	0.40±1.17
150	1.27±1.15	0.76±1.20	0.50±1.23	0.36±1.25
200	1.21±1.13	0.71±1.17	0.46±1.19	0.33±1.21
250	1.16±1.10	0.67±1.14	0.44±1.15	0.31±1.16
300	1.09±1.14	0.62±1.19	0.40±1.21	0.28±1.22

MMAD mass median aerodynamic diameter, *GSD* geometric standard deviation

aggregates to encapsulate anticancer therapeutic agent (5-fluorouracil) (22). In the current study, magnetic aggregates were examined for their regional aerosol deposition using a mNGI setup.

Primarily, we investigated the ability of PPG-NH2 and polyrotaxane to encapsulate Fe_3O_4 magnetic nanoparticles. The FTIR (Fig. 1) and TGA (Fig. 2) profiles indicated the surface adsorption of PPG-NH2 and polyrotaxane on magnetic iron oxide nanoparticles. The first stage of weight loss occurred in the temperature range between 125°C and 225°C, which is attributed to the loss of water molecules. Significant weight loss was observed for the polymer-coated samples at a temperature above 225°C. Thermal decomposition happened gradually with a T_{max} value of 245°C, and this could be referred to the decomposition of beta cyclodextrin residues. The observed temperature range for decomposition of polyrotaxanes is 225–310°C, which is consistent with the reported values (37).

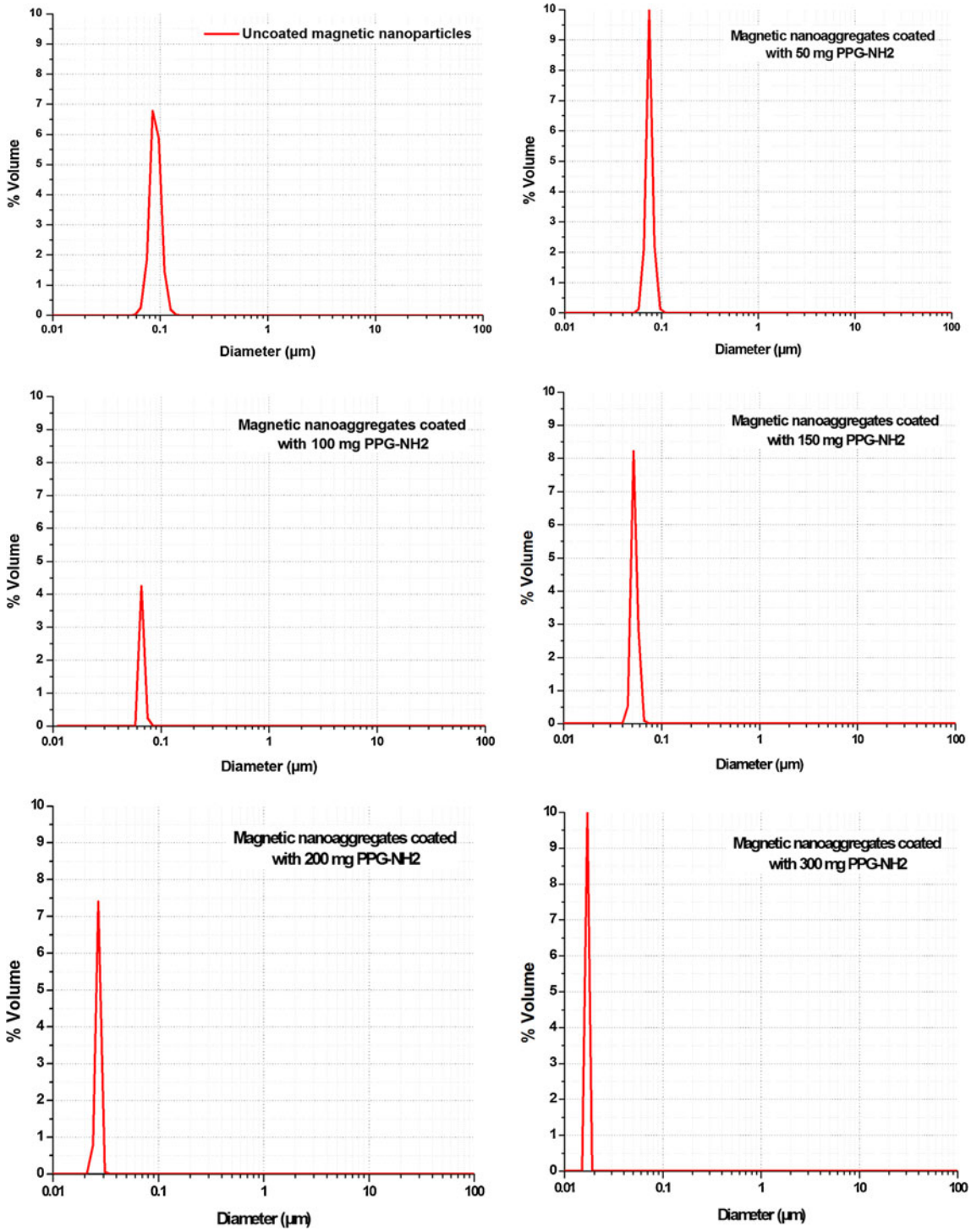

Fig. 3. Raw data for particle size measurements

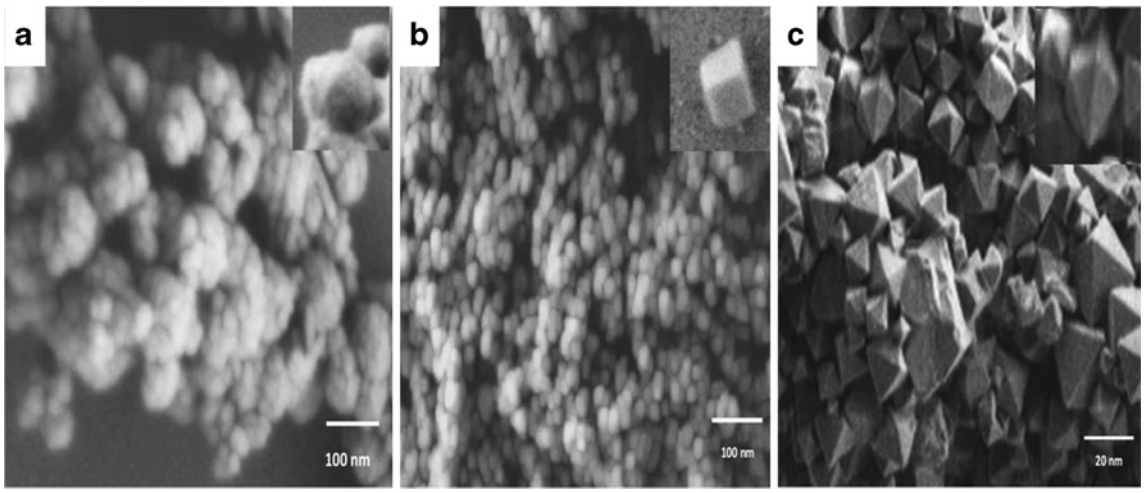

Fig. 4. FESEM images showing the difference in particles' morphology. **a** PPG-NH2-coated spherical, **b** cubic and **c** rhombic dodecahedron-polyrotaxane-coated magnetic aggregates of nanoparticles

The FTIR data verified the ability of both polymers to encapsulate magnetic nanoparticles at the examined concentrations (Fig. 1). Surface-modified polyrotaxane-coated magnetic aggregates revealed a broad band in the range between 1,000 and 1,300 cm^{-1}; this could be due to the stretching of the ether bond of beta cyclodextrin. In addition, some of these bands correspond to the vibrations of polypropylene oxide chains of PPG-NH2. The FTIR data of magnetic aggregates coated with amine functionalized polyrotaxane confirmed that magnetic nanoparticles were surrounded with PPG-NH2 and beta cyclodextrin polymers.

Particle Size and Morphology. Addition of PPG-NH2 or polyrotaxane seemed to significantly affect the particle size and morphology. Increasing the concentration of both polymers resulted in reduction in the particles' geometric diameters (Table II), which could be related to the content of Fe_3O_4 in the obtained aggregates. Upon screening the particle size, it was observed that all magnetic samples revealed a mono-disperse size distribution (Fig. 3). The polydispersity index for PPG-NH2-coated magnetic aggregates ranged from 0.08 to 0.29. An exemplarily TEM image for spherical magnetic PPG-NH2 aggregates is presented in Figure S-1. In addition, magnetic aggregates coated with polyrotaxane presented a morphological transformation from spherical to cubic shape (Fig. 4). The change in morphology could be referred to the rapid consumption of Fe3O4/polyrotaxane nuclei, due to the increased rate of crystal growth (38,39). Figure 5 demonstrates a comparative SEM image for the aggregates of spherical magnetic nanoparticles and those of cubic magnetic nanoparticles. As seen in the images, no significant difference is observed between both cases.

XRD and Estimation of {200}/{110} Crystal Plane Ratio. Comparing the X-ray diffraction (XRD) patterns of synthesized magnetic nanoparticles with the standard diffraction spectrum (Aldrich catalogue: 31,006-9) revealed that the synthesized products showed a crystalline Fe_3O_4. The five characteristic peaks for Fe_3O_4 were found at 2-theta angles of 30.95°, 35.89°, 44.34°, 55.06°, and 64.51°. These five peaks correspond to the diffraction from the 110, 200, 211, 220, 310, and 311 planes of face-centered cubic iron oxide crystals. Results for the nanoparticles size data computed by Scherrer's equation (40) are summarized in Table I. Addition of PPG-NH2 or polyrotaxane was usually associated by more organized nanostructures. The XRD patterns of magnetic aggregates with different crystal morphologies are shown in Fig. 6.

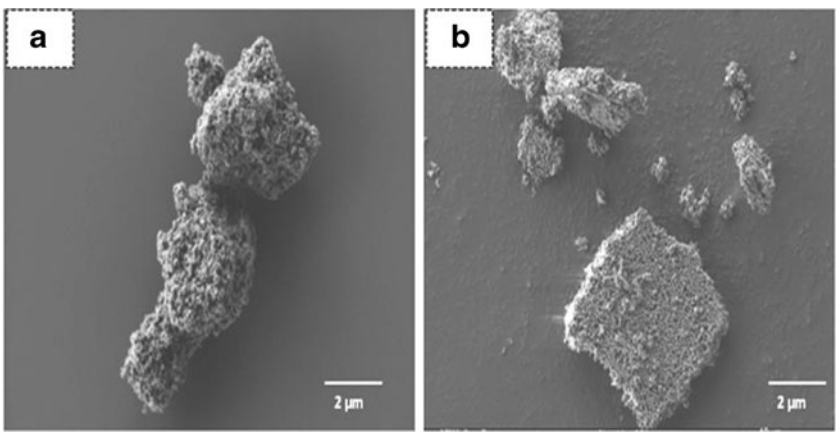

Fig. 5. SEM images of aggregates of spherical magnetic nanoparticles (**a**) and aggregates of cubic magnetic nanoparticles (**b**)

a

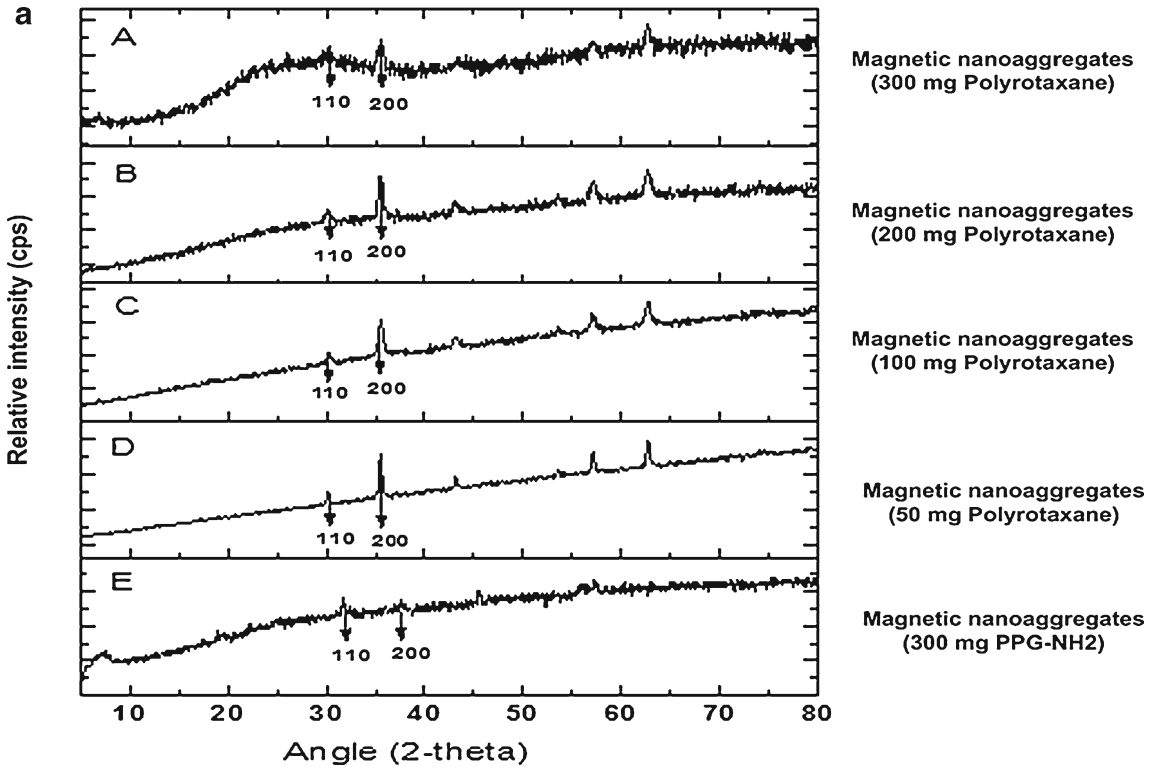

b

Polyrotaxane concentration (mg / 100 mg nanoparticles)	Crystal morphology	{200}/{110} Ratio
50	Cubic	0.96
100	Truncated cubic	1.04
150	Truncated rhombic	1.38
200	Regular rhombic	1.48
300	Rhombic dodecahedron	1.71

Fig. 6. XRD patterns of magnetic nanoaggregates coated with different surface coatings (**a**) and the predicted crystal morphologies for different magnetic aggregates (**b**)

The calculated {200}/{110} diffraction planes ratio helped in estimation of the magnetic crystal structure. For PPG-NH2-coated magnetic aggregates, the diffraction planes ratios are generally less than 0.5, which confirms the observed spherical morphology. However, polyrotaxane-coated aggregates demonstrated higher crystal plane ratios, which indicates the transformation in the crystal morphology from cubic to dodecahedron.

Saturation Magnetization of Aggregates as Measured with Vibrating Sample Magnetometer. The relation between the induced moment of magnetic samples and the applied magnetic field is presented in Fig. 7. The measured saturation magnetization value was 0.32 emu/g. This saturation magnetization value was much smaller than the literature value for magnetite (4,20), which could be attributed to the smaller size of magnetic nanoparticles or the surface oxidation of magnetite at the surface of nanoparticles. Polyrotaxane-coated samples showed a saturation magnetization value 3.56 emu/g, which could be referred to the surface coverage of aggregates with polyrotaxane inclusion complex.

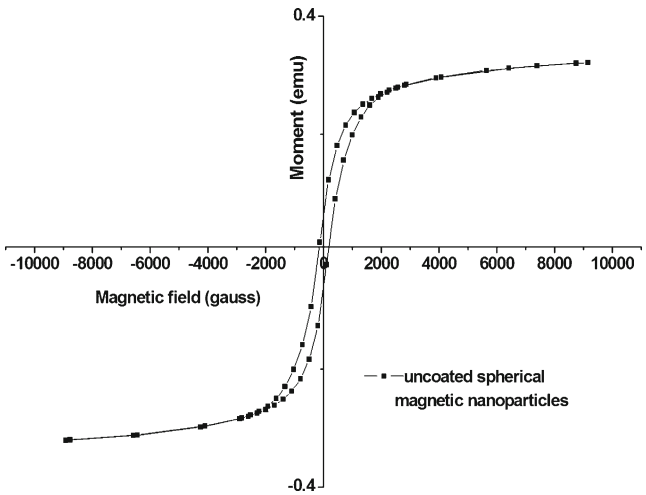

Fig. 7. Hysteresis loop for uncoated spherical magnetic nanoparticles of magnetite (Fe_3O_4)

Selection of a Dry Powder Inhaler Device for Magnetic Aerosol Delivery. The selection of an inhaler device for delivery of magnetic aggregates was based on preliminary experiments conducted using two proposed inhaler devices: the Handihaler® and Aerolizer®. The internal geometries for both devices are demonstrated in Fig. 8. Based on our observations, the Handihaler® demonstrated better dispersion and less capsule and device retention. This could be attributed to the different mechanisms of operation of both inhaler devices (41). The Handihaler® exhibits different mechanism of operation, which showed impact on the fine particle fraction (FPF) and emitted dose (ED).

In case of the Aerolizer®, the airflow enters the inhaler device through the two opposite tangential inlets of the capsule chamber. The turbulent airflow is the only major factor that assists in capsule ejection. However, in case of the Handihaler®, the air stream passes through a single inlet in the inhaler device, and then the inhalation flow stream is suddenly expanded as it passes through the capsule chamber. The sudden opening during the air passage from the inlet to capsule chamber resulted in a pressure loss in this region associated with an annular circulation of air. The incoming flow of air pushes the capsule toward the grid simultaneously with the low-pressure regions that are continuously attracting the capsule toward the grid. The alternating attraction and pushing causes the capsule to spin and vibrate in the chamber. For this reason, better capsule evacuation is obtained in case of the Handihaler®.

Application of Magnetic Next Generation Impinger for Estimation of Aerosol Deposition Characteristics. The deposition of coated magnetic aerosol particles in an *in vitro* lung model has been reported by Xie *et al.* (31). In the current study, the aerosolization performance of magnetic aggregates was examined using a magnetic next generation setup (Scheme 1). A preliminary experiment on a standard sample (MMAD=5 μm, GSD=1.83) was conducted in both NGI (42)

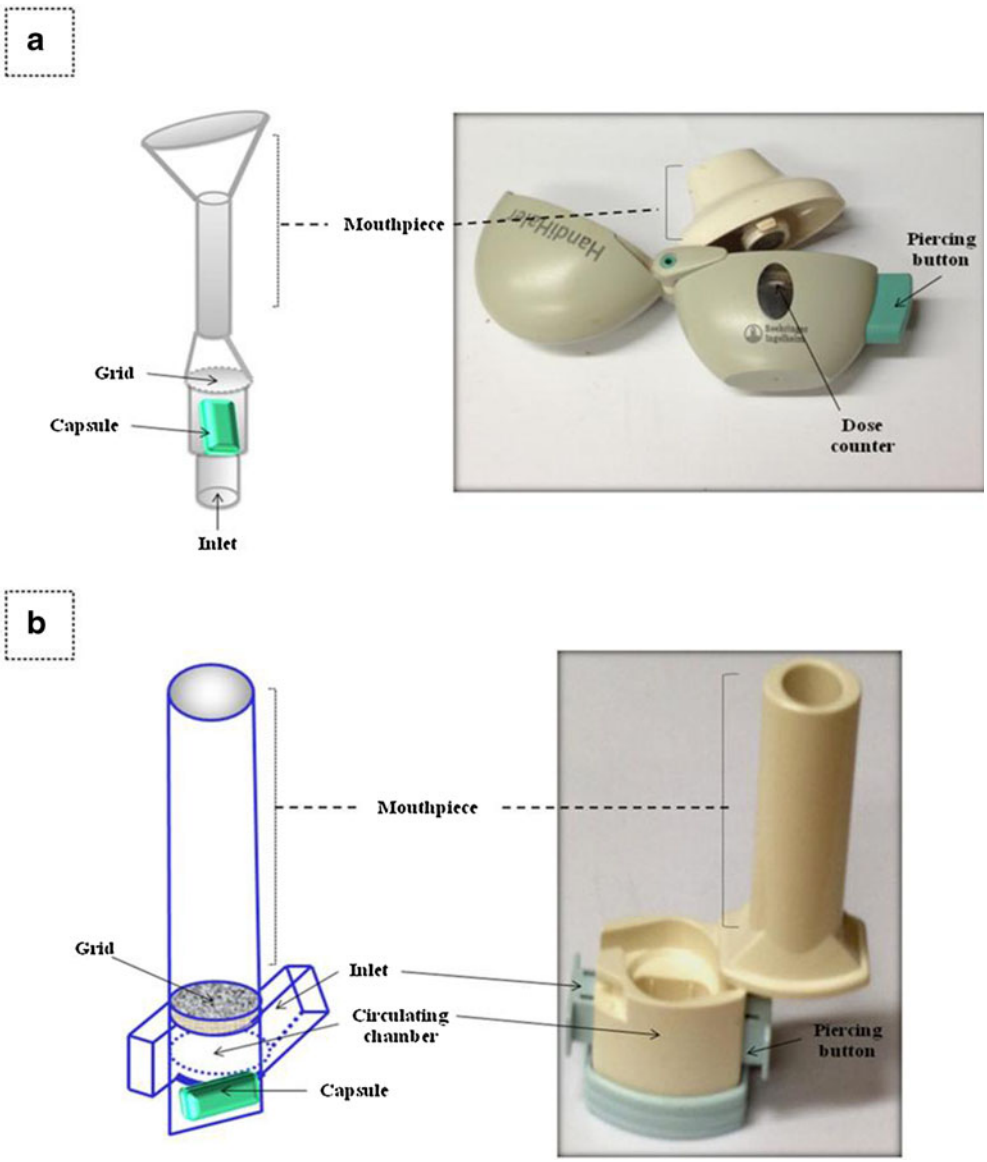

Fig. 8. Images and schematic views of the two examined dry powder inhalation devices: Handihaler® (**a**) and Aerolizer® (**b**). The internal geometry of both devices is based on structures illustrated in (41)

and mNGI in order to validate the cut-off diameters for each stage of magnetic setup. The results obtained indicate similarity in MMAD and GSD values measured in both devices, which suggests that the modifications made to NGI have not significantly affected its particle sizing capabilities.

Different samples were examined for their magnetic aerosol deposition at variable flow rates. The dependence of magnetic field on the position of the permanent magnet (1 T) is presented in Fig. 9. Generally, the magnetic field showed a two-fold increase on increasing the inhalation flow rate from 15 to 100 L/min. At 60 L/min, the average magnetic field at mNGI stages 1 (cut-off diameter higher than 4.46 μm) was 0.088 T. In comparison, at cut-off diameter less than 4.46 μm, the average magnetic field approximately increased from 0.22 to 0.731 T upon moving from stage 2 to stage 7.

The aerosol deposition performance of polymer-coated magnetic aggregates was presented in Figs. 10, 11, and 12. In these figures, the fractional mass deposition of nanoparticles was plotted *versus* the upper cut-off diameter of each impinger stage. The aerosol deposition performance for each sample was qualified based on calculation of two parameters; the fine particle dose and the FPF.

Effect of Flow Rate on Magnetic Aerosol Deposition. Generally, the samples coated with PPG-NH2 showed a unimodal particle size distribution (Figs. 10 and 11). However, polyrotaxane-coated samples induced bimodality in the size distribution profile (Fig. 12). The observed bimodality for the polyrotaxane-coated samples (from 50 to 150 mg polyrotaxane/100 mg nanoparticles) reflects greater fraction of aggregates for these samples,

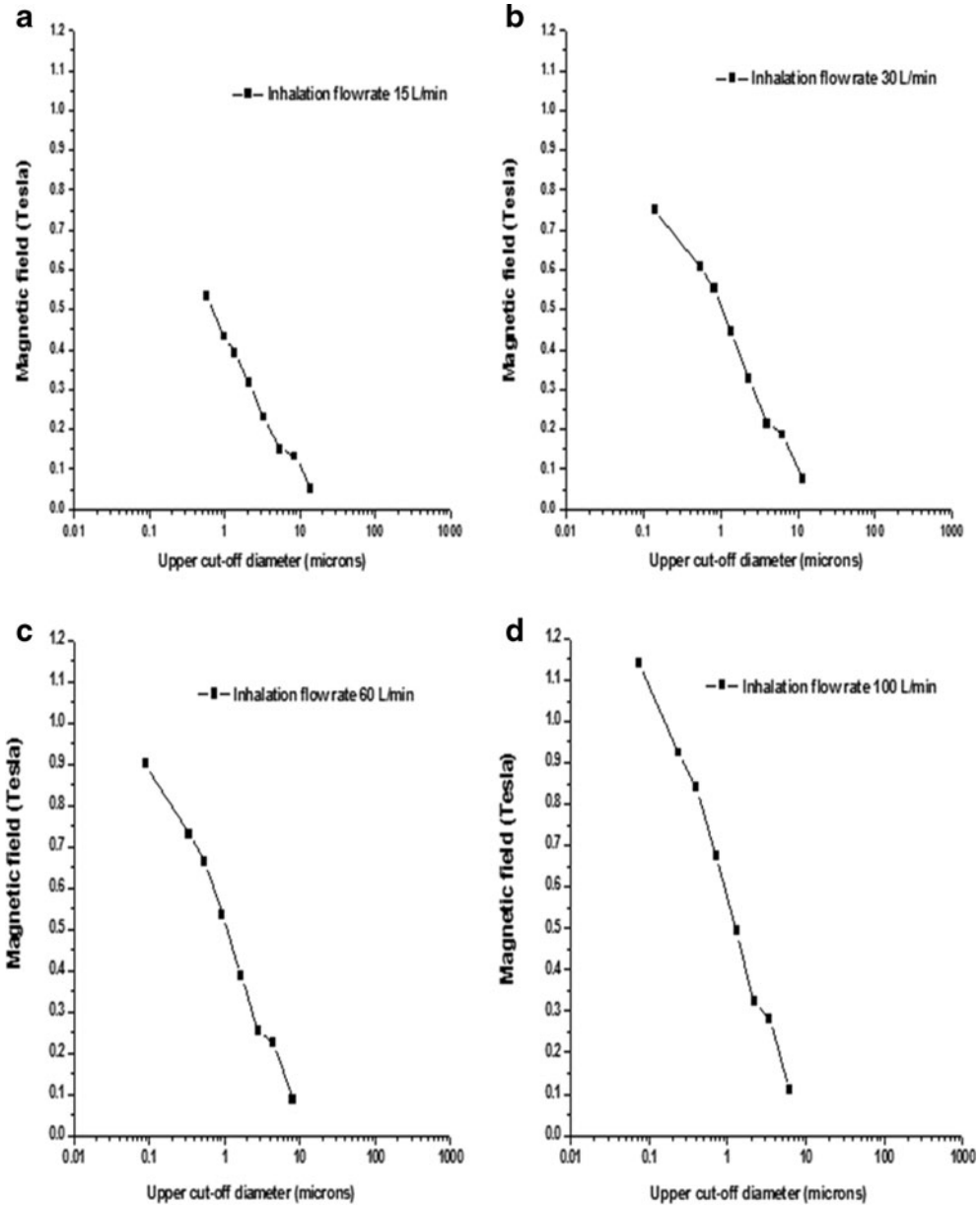

Fig. 9. Effect of air flow rate on the measured magnetic field values on each stage of magnetic next generation impinger

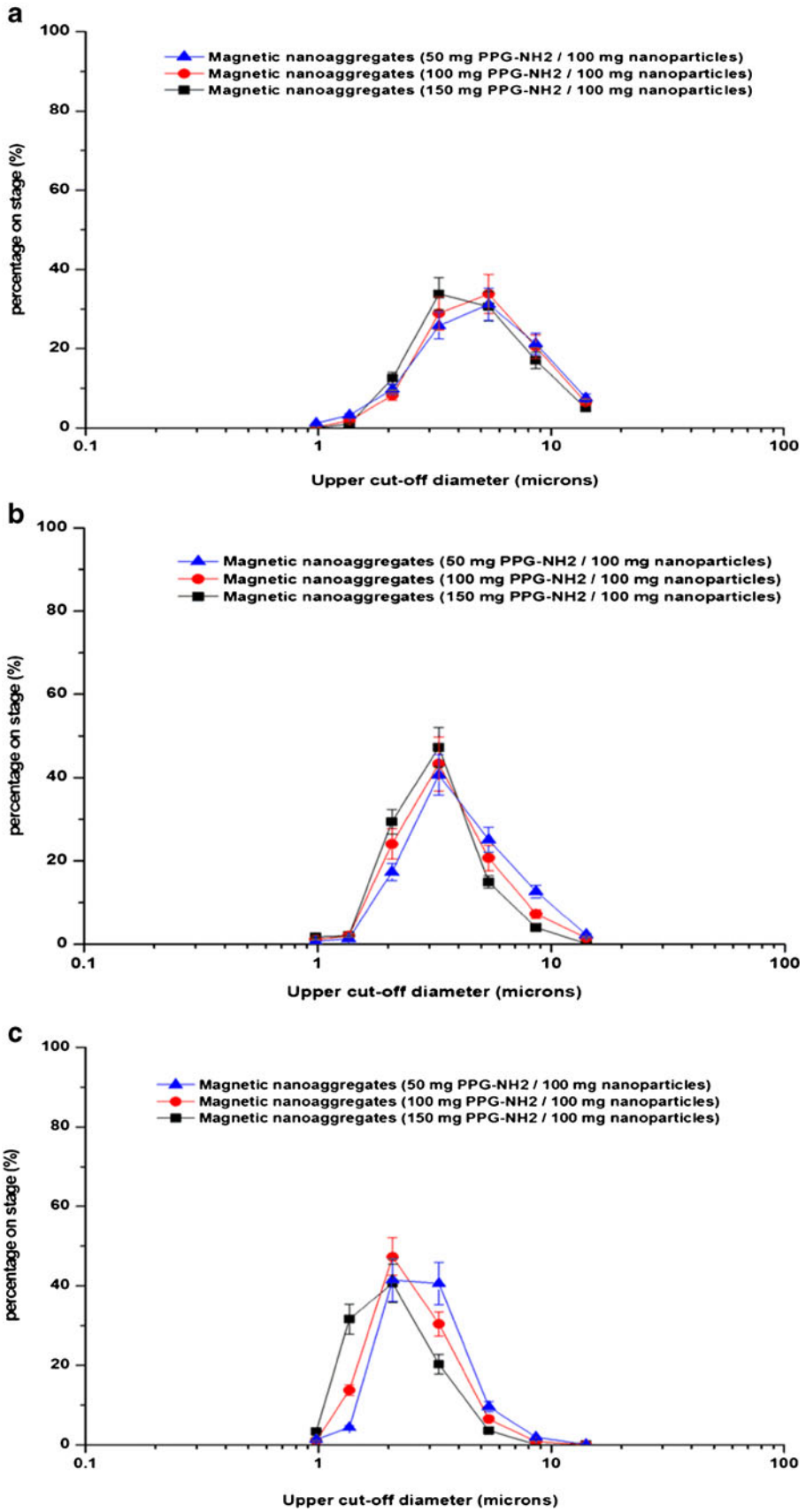

Fig. 10. Effect of poly(propylene glycol) bis(2-aminopropylether) (PPG-NH2) on the percentage aerosol deposition on mNGI. The mass deposition on each stage was measured at 15 L/min (**a**), 30 L/min (**b**), and 60 L/min (**c**)

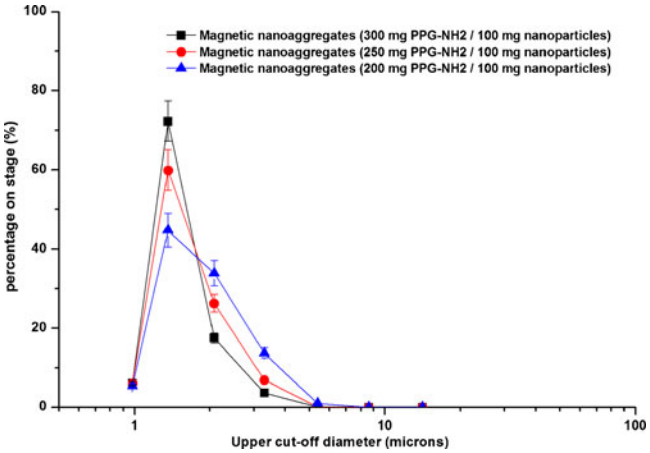

Fig. 11. Magnetic *in vitro* aerosol deposition of magnetic aggregates coated with higher concentrations of poly(propylene glycol) bis(2-aminopropylether) "PPG-NH2" and measured at 60 L/min

which is diminished upon increasing the coating polymer concentration.

The inhalation flow rate seemed to have significant impact on magnetic aerosol deposition (Fig. 11). This effect could be attributed to the improved dispersion behavior as a result of the increased turbulence and decreased capsule and device retention. PPG-NH2-coated samples showed major aerosol deposition between stages 1 and 4, which suggests poor dispersion behavior for the aggregates. The calculated MMAD values for PPG-NH2- and polyrotaxane-coated magnetic nanoparticles are listed in Tables I and II, respectively. These values indicate the dual dependence of magnetic aerosol deposition on the inhalation flow rate and crystal morphology.

Effect of Polymer Concentration on the Calculated FPF and ED. The increase in the FPF was significant between 15 and 30 L/min for both spherical and cubic aggregates, where an increase in the FPF from 36.28% to 43.39% and

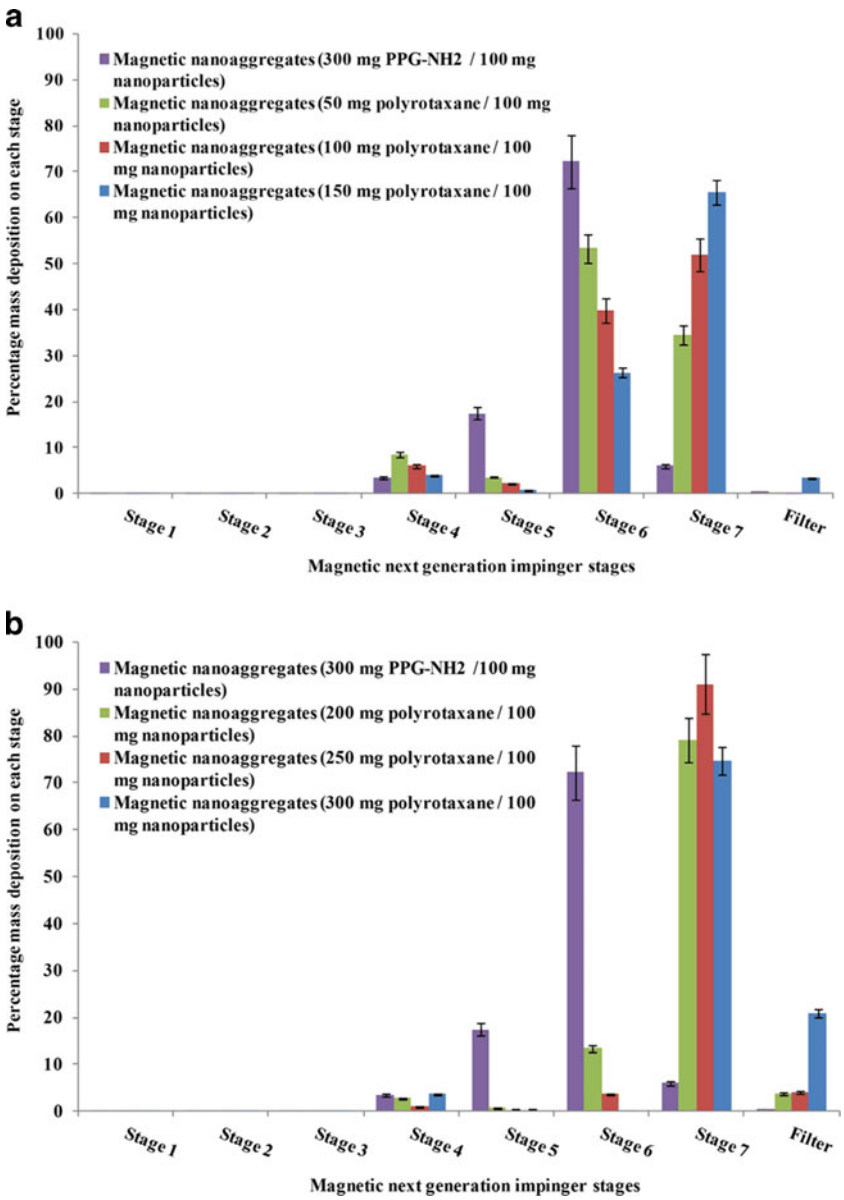

Fig. 12. Bimodal (**a**) and unimodal (**b**) *in vitro* aerosol deposition of polyrotaxane-coated magnetic aggregates measured at 60 L/min

from 54.57% to 67.10% was observed for the 50- and 150-mg PPG-NH2-coated samples, respectively (Table III). To the author's knowledge, no comparative data exist for magnetic aggregates. The same observation obtained upon increasing the flow rate from 30 to 60 L/min (Table S-2). A further increase in inhalation flow rate from 60 to 100 L/min shows no significant effect on the FPF of magnetic samples. Nevertheless, a significant reduction in the percentage emitted dose was observed for the sample coated with 300 mg of PPG-NH2 (Table III). This could be attributed to the reduction in the Fe_3O_4 content as compared to the polymer, which resulted in less magnetic collection.

The magnetic formulation coated with 100 mg PPG-NH2/100 mg nanoparticles showed a polydispersity index of 0.12 (Table I), which is reflected on the FPF and ED. The calculated MMAD for this sample is 2.97 μm, and the GSD is 1.41. The decreased value of the polydispersity index is only reflected on the GSD, which means lower deposition of particles in stages 1 and 2 of NGI. This can be reflected in lowering the mouth and throat deposition of inhaled powders following their *in vivo* administration. However, the sample coated with 250 mg of PPG-NH2 showed a comparable value of polydispersity index and a greater deep aerosol deposition (indicated by the lower value of MMAD). This is because the aerosol deposition is a complex function of the particle size and size distribution profile.

Dependence of Magnetic Aerosol Deposition on Individual Particle's Magnetization. The individual particle's magnetization was calculated based on the experimentally measured saturation magnetization data and the mass distribution profiles determined using mNGI (Fig. 13). The dependence of particles' saturation magnetization on their diameters was previously reported (43,44). The magnetic moment distribution per each particle was calculated and plotted *versus* the cut-off diameter of mNGI and presented in Figs. 14, 15, and 16. Our results are in agreement with the previously validated data (44). The magnetic moment followed an exponential distribution as a function of the upper cut-off diameters of mNGI (R^2=0.9974). Increasing the saturation magnetization of magnetic aggregates samples from 0.32 to 1.16 emu/g resulted in a shift in the saturation magnetization distribution, primarily toward the lower stages of impinger. This shift could be attributed in the increased retention by the magnetic field (1 Tesla) in the stages with cut-off diameters <4.46 μm. These

Table III. Percentages Fine Particle Fraction and Emitted Dose of Different PPG-NH2, Poly(propylene glycol) bis(2-Aminopropylether), Coated Magnetic Aggregates Measured in Magnetic Next Generation Impinger

PPG-NH2 concentration (mg)	Percentage fine particle fraction (%) 60 L/min	Percentage emitted dose (%) 60 L/min
0	35.88	40.32
50	49.98	51.99
100	59.4	60.35
150	69.67	70.78
200	64.97	65.95
250	52.98	53.21
300	44.99	45.56

PPG-NH2 poly(propylene glycol) bis(2-aminopropylether)

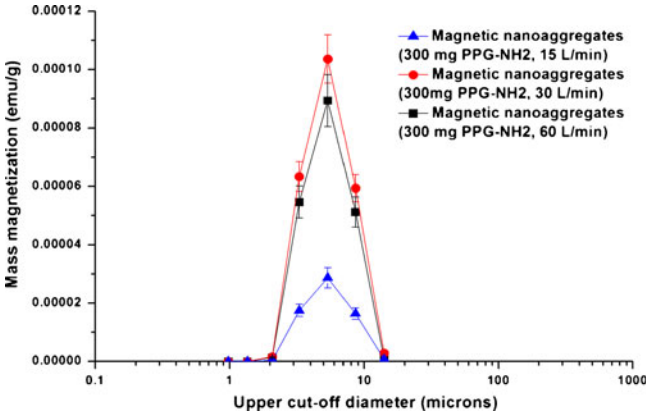

Fig. 13. The influence of airflow rate on the distribution of saturation magnetization per each stage of mNGI for magnetic aggregates samples coated with variable amounts of PPG-NH2/100 mg nanoparticles

results suggest better deposition in the lower stages of impinger upon increasing the magnetization of the prepared magnetic samples.

Interestingly, a shift in the mass magnetization distribution profile toward the upper stages of mNGI was observed for the sample prepared with 1.51 μm MMAD and 1.21 GSD (measured at 15 L min^{-1}). This shift could be attributed to the higher particle magnetization which may lead to an increased particles' aggregation. An increase in the inhalation flow rate from 15 to 30 L min^{-1} resulted in a change in the magnetization distribution profile showing an increased positive slope with the upper cut-off diameter of mNGI. Further increase in the inhalation flow rate from 30 to 60 L min^{-1} resulted in a significant shift in the magnetization profile toward the upper stages of impinger. This could be primarily attributed to the reduced exposure time to the magnetic field gradient, as the inhalation flow rate increased. The results illustrated above indicate the direct proportionality between the individual particle magnetization and the amount of magnetic field applied (position of nanoparticles on different stages of mNGI relative to the magnet), when the particles' MMAD is smaller than 3.37 μm.

Mathematical Modeling of the Dispersion Process. A powder deaggregation index was proposed and calculated by dividing the geometric diameter of powder aggregates (measured by the dynamic light scattering technique) by the MMAD (estimated from the magnetic aerosol deposition data). Thereafter, a flow rate titration was performed for the calculated deaggregation index. The deaggregation index-flow rate curves showed a sigmoid profile, which can be perfectly fitted to Eq. 2. The calculated kinetic parameters for polyrotaxane-coated samples are exemplarily presented in Table IV. The efficiency of the dispersion process was expressed as parameter (a) in Eq. 2. The calculated values for parameter (a) ranged between 0.13 and 0.32 for the samples coated with PPG-NH2 (in the concentration range from 50 to 150 mg/100 mg nanoparticles), which indicates incomplete powder dispersion by the inhaler device. Significant increase in parameter (a) values was detected for the samples coated with high concentrations of PPG-NH2 (more than 150/100 mg nanoparticles) and polyrotaxane (in the concentration range from 50 to 300/100 mg nanoparticles). The reduction in parameter (a) values indicates the ability of the inhaler

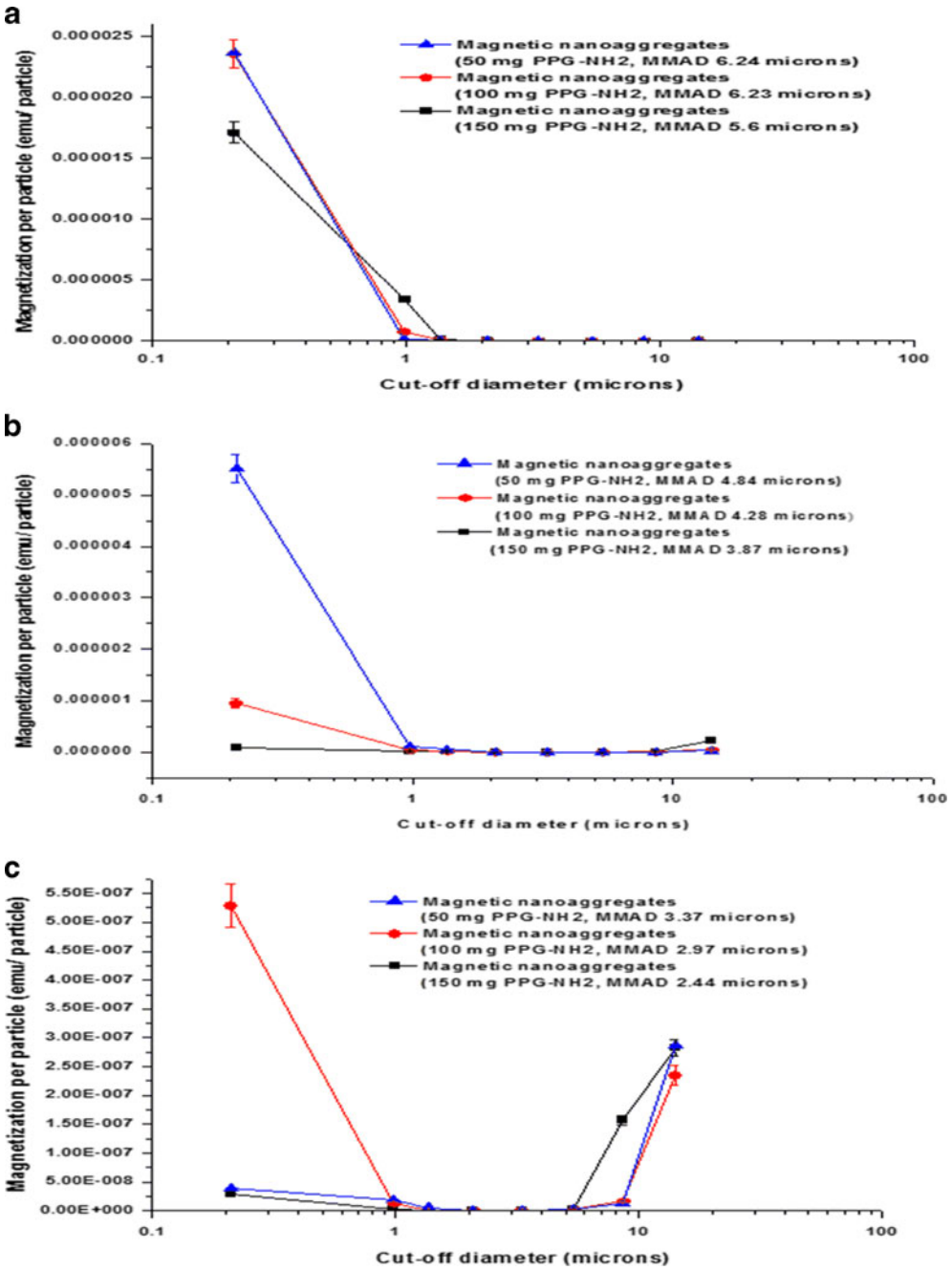

Fig. 14. The influence of airflow rate on the magnetization per particle (emu/particle) measured in mNGI at 15 L/min (**a**), 30 L/min (**b**), and 60 L/min (**c**) for magnetic aggregates coated with variable amounts of PPG-NH2/100 mg nanoparticles

device together with the applied magnetic field to approximately achieve complete powder dispersion of the aggregates into primary particles.

The rate and extent of the dispersion process was expressed by parameters (b) and (x_0), respectively. The presence of coating polymer on the surface of magnetic nanoparticles affects the force required to break up the aggregates into primary particles, which consequently affects the rate of dispersion process. Polyrotaxane-coated magnetic aggregates showed better dispersion behavior, which is indicated by the higher values of parameter (b). The highest dispersion was observed for the sample coated with 300 mg of polyrotaxane/100 mg nanoparticles with a parameter (a) value of 0.98 and parameter b value of 27.59. A reduced parameter (b) value indicates the possibility of powder dispersion at relatively lower air flow rates. TEM images showing the dispersion process as a function of air flow rate were presented in Fig. S-2.

DISCUSSION

The morphological change associated with the addition of polyrotaxane can be attributed to the increased rate of crystal growth. It is well known that increasing the growth rate is

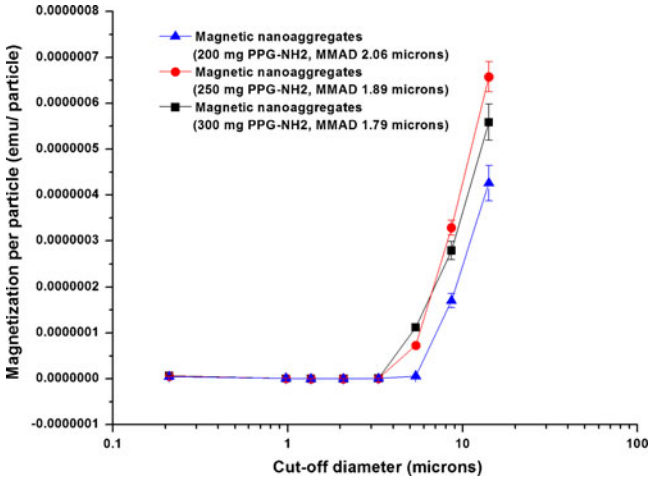

Fig. 15. Exponential increase in particle's magnetization upon moving toward the mNGI stages with higher cut-off diameter. This exponential profile is valid only for samples with MMAD less than 3 μm

always associated with a rapid consumption of small nuclei of Fe_3O_4/PR. Therefore, the morphology will be forced toward the cubic shape nanoparticles (38,39). Our results indicate a significant reduction in the particle size of cubic magnetic nanoparticles upon increasing the concentration of polyrotaxane (from 50 to 300 mg). This can be also confirmed by the peak broadening in the X-ray diffraction pattern (Fig. 6). Results for the particle size distribution in mNGI suggest the dependence of *in vitro* aerosol deposition on the applied inhalation flow rate, which is confirmed by previously reported studies (45,46). Therefore, we applied a flow rate titration for investigation of the kinetics of dispersion process. Measurement of the dispersion behavior of powders at a sequence of air flow rates was previously investigated (36). In the current study, we modified the method proposed in the literature (36) by estimating a novel deaggregation index based on the data obtained from the mNGI. Different samples can be compared based on the maximum extent of dispersion achieved

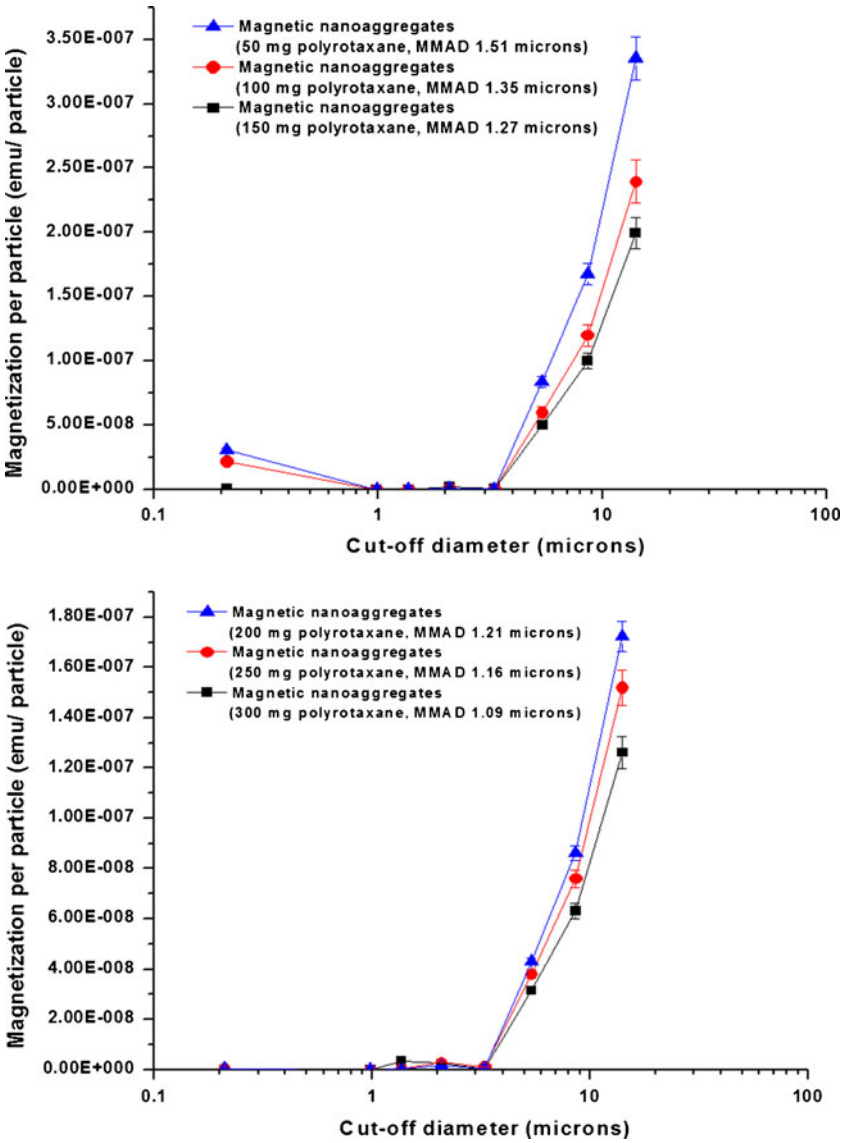

Fig. 16. The estimated particle's magnetization for magnetic nanoaggregates prepared with variable amounts of polyrotaxane/100 mg nanoparticles. The samples were examined using mNGI operated at 60 L/min

Table IV. The Estimated Parameters for the Mathematical Curve Fitting of Deaggregation Index-Air Flow Rate Profiles for Polyrotaxane-Coated Magnetic Aggregates Compared to the Uncoated Magnetic Fe_3O_4 Nanoparticles

Polyrotaxane concentration mg/100 mg nanoparticles	a	b	x_0
0	0.14	33.44	34.31
50	0.78	28.67	40.49
100	0.77	27.59	42.15
150	0.92	27.85	42.03
200	0.92	27.14	42.45
250	0.94	22.12	44.31
300	0.98	18.68	45.07

at 100 L/min. Therefore, the estimated deaggregation indices can be seen as a valuable tool for the potential development of magnetic dry powders for inhalation.

The change in the individual particle's morphology is not reflected on the aggregates shape (Fig. 5), and it only affects the deaggregation behavior upon exposure to an airflow stream. Based to our knowledge, the shape of aggregates has an impact on their aerodynamic drag forces and considerably affects their entrainment in air stream. Previous mathematical studies were conducted to describe the effect of drag forces on the local aerosol deposition of nanoparticles (31). The transport and deposition equation of magnetic aerosols can be written:

$$\frac{d_v}{d_t} = \frac{f}{\tau_p}(u_i - v_i) + g_i(1-\alpha) + f_{\text{Brownian},i} + f_{M,i} \qquad (3)$$

where v_i and u_i are the components of the particle and local flow velocity, respectively. τ_p is the characteristic time required for the particle to respond to changes in fluid motion. The local deposition of particles in a model respiratory tract is affected by gravitational forces (g_i), Brownian motion (f_{brownian}), and drag factor (f). Based on the SEM imaging, we assumed that aggregates have similar shape. Nevertheless, evaluation of the aggregate geometries is needed for the development of geometric shape factor that can be used in drag coefficient calculations, which is an interesting area of research for perspective studies.

On the other hand, the variation in the dispersion process between cubic and spherical nanoparticles could be connected to the different fractal geometry of individual particles (47). The change in the geometric network structures results in variations in the work of adhesion between primary neighboring particles (48). Therefore, the air flow rate and magnetic field can influence the dispersion behavior of magnetic aggregates with different fractal geometries.

CONCLUSION

Variation of coating polymer concentrations can be regarded as a primary factor for controlling the particle size, shape, and dispersion behavior of magnetic aggregates. The change in the particle size concurrently with the particle shape can suggest the moderate rate of thermal decomposition of iron precursor, thus giving sufficient time for the formation of aggregates. In the current study, we demonstrated the morphological transformation of polymeric-coated magnetic aggregates from spherical to rhombic passing through the cubic crystal structure.

In addition, we introduced a modified setup of the next generation impinger for investigating the *in vitro* aerosol deposition of magnetic nanoparticles. The magnetic deposition of polymeric-coated magnetic aggregates seemed to be complex and dependent on various interactive factors. Therefore, we investigated the dispersion profile of different aggregate samples and showed how it was affected by the magnetization value on each particle. Mathematical modeling of the *in vitro* dispersion profile leads to better selection of the ideal formulation, which provides high deaggregation index at relatively low air flow rate.

ACKNOWLEDGMENTS

This work was supported by the Pharmaceutical Crystallization and Control of Drug Laboratory, Department of Chemical and Biochemical Engineering, Faculty of Engineering, University of Western Ontario, London, Ontario, Canada.

Conflict of Interest The authors declare no conflict of interest in this work.

REFERENCES

1. Brzoska M, Langer K, Coester C, Loitsch S, Wagner TOF, Mallinckrodt C. Incorporation of biodegradable nanoparticles into human airway epithelium cells—in vitro study of the suitability as a vehicle for drug or gene delivery in pulmonary diseases. Biochem Biophys Res Commun. 2004;318(2):562–70.
2. Grenha A, Seijo B, Remuñán-López C. Microencapsulated chitosan nanoparticles for lung protein delivery. Eur J Pharm Sci. 2005;25(4–5):427–37.
3. Duguet E, Vasseur S, Mornet S, Devoisselle JM. Magnetic nanoparticles and their applications in medicine. Nanomedicine (Lond). 2006 Aug;1(2):157–68.
4. Gupta AK, Naregalkar RR, Vaidya VD, Gupta M. Recent advances on surface engineering of magnetic iron oxide nanoparticles and their biomedical applications. Nanomedicine (Lond). 2007 Feb;2(1):23–39.
5. Arias JL, Gallardo V, Gómez-Lopera SA, Plaza RC, Delgado AV. Synthesis and characterization of poly(ethyl-2-cyanoacrylate) nanoparticles with a magnetic core. J Controlled Release. 2001;77(3):309–21.
6. Stahlhofen W, Moller W. Behaviour of magnetic micro-particles in the human lung. Radiat Environ Biophys. 1993;32(3):221–38.
7. Choi H, Choi SR, Zhou R, Kung HF, Chen IW. Iron oxide nanoparticles as magnetic resonance contrast agent for tumor imaging via folate receptor-targeted delivery. Acad Radiol. 2004 Sep;11(9):996–1004.
8. Pauwels EK, Erba P. Towards the use of nanoparticles in cancer therapy and imaging. Drug News Perspect. 2007 May;20(4):213–20.
9. Bamrungsap S, Chen T, Shukoor MI, Chen Z, Sefah K, Chen Y, *et al.* Pattern recognition of cancer cells using aptamer-conjugated magnetic nanoparticles. ACS Nano. 2012;6(5):3974–81.
10. Lewin M, Carlesso N, Tung C, Tang X, Cory D, Scadden DT, *et al.* Tat peptide-derivatized magnetic nanoparticles allow in vivo tracking and recovery of progenitor cells. Nat Biotech. 2000;18(4):410–4.
11. Hood JD, Bednarski M, Frausto R, Guccione S, Reisfeld RA, Xiang R, *et al.* Tumor regression by targeted gene delivery to the neovasculature. Science. 2002;296(5577):2404–7.

12. Hua MY, Yang HW, Liu HL, Tsai RY, Pang ST, Chuang KL, *et al*. Superhigh-magnetization nanocarrier as a doxorubicin delivery platform for magnetic targeting therapy. Biomaterials. 2011 Dec;32(34):8999–9010.
13. Lam JK, Liang W, Chan H. Pulmonary delivery of therapeutic siRNA. Adv Drug Deliv Rev. 2012;64(1):1–15.
14. Pankhurst QA, Thanh NTK, Jones SK, Dobson J. Progress in applications of magnetic nanoparticles in biomedicine. J Phys D. 2009;42(22):224001.
15. McCarthy JR, Kelly KA, Sun EY, Weissleder R. Targeted delivery of multifunctional magnetic nanoparticles. Nanomedicine (Lond). 2007 Apr;2(2):153–67.
16. Zhang JL, Srivastava RS, Misra RD. Core-shell magnetite nanoparticles surface encapsulated with smart stimuli-responsive polymer: synthesis, characterization, and LCST of viable drug-targeting delivery system. Langmuir. 2007;23(11):6342–51.
17. Bogdanov Jr AA, Martin C, Weissleder R, Brady TJ. Trapping of dextran-coated colloids in liposomes by transient binding to aminophospholipid: preparation of ferrosomes. Biochim Biophys Acta. 1994 Jul 13;1193(1):212–8.
18. Bulte JW, De Cuyper M. Magnetoliposomes as contrast agents. Methods Enzymol. 2003;373:175–98.
19. Tomitaka A, Koshi T, Hatsugai S, Yamada T, Takemura Y. Magnetic characterization of surface-coated magnetic nanoparticles for biomedical application. J Magn Magn Mater. 2011;323(10):1398–403.
20. Gupta AK, Gupta M. Synthesis and surface engineering of iron oxide nanoparticles for biomedical applications. Biomaterials. 2005;26(18):3995–4021.
21. Walter JG, Petersen S, Stahl F, Scheper T, Barcikowski S. Laser ablation-based one-step generation and bio-functionalization of gold nanoparticles conjugated with aptamers. J Nanobiotechnology 2010;8:21-3155-8-21.
22. Ragab DM, Rohani S, Consta S. Controlled release of 5-fluorouracil and progesterone from magnetic nanoaggregates. Int J Nanomedicine. 2012;7:3167–89.
23. Lipka J, Semmler-Behnke M, Sperling RA, Wenk A, Takenaka S, Schleh C, *et al*. Biodistribution of PEG-modified gold nanoparticles following intratracheal instillation and intravenous injection. Biomaterials. 2010 Sep;31(25):6574–81.
24. Siegwart DJ, Srinivasan A, Bencherif SA, Karunanidhi A, Oh JK, Vaidya S, *et al*. Cellular uptake of functional nanogels prepared by inverse miniemulsion ATRP with encapsulated proteins, carbohydrates, and gold nanoparticles. Biomacromolecules. 2009;10(8):2300–9.
25. Harada A, Okada M, Li J, Kamachi M. Preparation and characterization of inclusion complexes of poly(propylene glycol) with cyclodextrins. Macromolecules. 1995;28(24):8406–11.
26. Zhou Y, Wang H, Wang C, Li Y, Lu W, Chen S, *et al*. Receptor-mediated, tumor-targeted gene delivery using folate-terminated polyrotaxanes. Mol Pharmaceutics. 2012;9(5):1067–76.
27. Moghimi SM, Hedeman H, Christy NM, Illum L, Davis SS. Enhanced hepatic clearance of intravenously administered sterically stabilized microspheres in zymosan-stimulated rats. J Leukoc Biol 54:513–7.
28. Weiss RB, Donehower RC, Wiernik PH, Ohnuma T, Gralla RJ, Trump DL, *et al*. Hypersensitivity reactions from taxol. J Clin Oncol 1990;8:1263–8.
29. Mykhaylyk O, Dudchenko N, Dudchenko A. Doxorubicin magnetic conjugate targeting upon intravenous injection into mice: high gradient magnetic field inhibits the clearance of nanoparticles from the blood. J Magn Magn Mater. 2005;293(1):473–82.
30. Azarmi S, Roa WH, Löbenberg R. Targeted delivery of nanoparticles for the treatment of lung diseases. Adv Drug Deliv Rev. 2008;60(8):863–75.
31. Xie Y, Longest PW, Xu YH, Wang JP, Wiedmann TS. In vitro and in vivo lung deposition of coated magnetic aerosol particles. J Pharm Sci. 2010;99(11):4658–68.
32. Ohno H, Yoshizawa M, Ogihara W. Development of new class of ion conductive polymers based on ionic liquids. Electrochim Acta. 2004;50(2–3):255–61.
33. Bosquillon C, Lombry C, Préat V, Vanbever R. Influence of formulation excipients and physical characteristics of inhalation dry powders on their aerosolization performance. J Controlled Release. 2001;70(3):329–39.
34. Hoe S, Young PM, Chan HK, Traini D. Introduction of the electrical next generation impactor (eNGI) and investigation of its capabilities for the study of pressurized metered dose inhalers. Pharmaceut Res 2009;26:431–7.
35. Hoe S, Traini D, Chan HK, Young P. Measuring charge and mass distributions in dry powder inhalers using the electrical Next Generation Impactor (eNGI). Eur J Pharm Sci. 2009;38:88–94.
36. Behara SRB, Larson I, Kippax P, Morton DAV, Stewart P. An approach to characterising the cohesive behaviour of powders using a flow titration aerosolisation based methodology. Chem Eng Sci. 2011;66(8):1640–8.
37. Suzaki Y, Murata S, Osakada K. Ferrocene-containing side chain polyrotaxanes obtained by radical copolymerization of styrenes with acrylamide with a 2]rotaxane structure. Chem Lett. 2009;38(4):356–7.
38. Zhen G, Muir BW, Moffat BA, Harbour P, Murray KS, Moubaraki B, *et al*. Comparative study of the magnetic behavior of spherical and cubic superparamagnetic iron oxide nanoparticles. J Phys Chem C. 2011;115(2):327–34.
39. Song Q, Zhang ZJ. Shape control and associated magnetic properties of spinel cobalt ferrite nanocrystals. J Am Chem Soc. 2004;126(19):6164–8.
40. Parsons JG, Luna C, Botez CE, Elizalde J, Gardea-Torresdey JL. Microwave assisted synthesis of iron(III) oxyhydroxides/oxides characterized using transmission electron microscopy, X-ray diffraction, and X-ray absorption spectroscopy. J Phys Chem Solids. 2009;70(3):555–60.
41. Donovan MJ, Kim SH, Raman V, Smyth HD. Dry powder inhaler device influence on carrier particle performance. J Pharm Sci. 2012;101(3):1097–107.
42. Mitchell JP, Nagel MW, Wiersema KJ, Doyle CC. Aerodynamic particle size analysis of aerosols from pressurized metered-dose inhalers: comparison of Andersen 8-stage cascade impactor, next generation pharmaceutical impactor, and model 3321 aerodynamic particle sizer aerosol spectrometer. AAPS PharmSciTech. 2003 Oct 22;4(4):E54.
43. Hori H, Yamamoto Y, Iwamoto T, Miura T, Teranishi T, Miyake M. Diameter dependence of ferromagnetic spin moment in Au nanocrystals. PhysRevB. 2004;69(17):174411.
44. He L. Comment on "Diameter dependence of ferromagnetic spin moment in Au nanocrystals". PhysRevB. 2010;81(9):096401.
45. Coates MS, Chan HK, Fletcher DF, Raper JA. Influence of air flow on the performance of a dry powder inhaler using computational and experimental analyses. Pharm Res. 2005 Sep;22(9):1445–53.
46. Coates MS, Chan HK, Fletcher DF, Raper JA. Effect of design on the performance of a dry powder inhaler using computational fluid dynamics. Part 2: air inlet size. J Pharm Sci. 2006 Jun;95(6):1382–92.
47. Lee C, Kramer TA. Prediction of three-dimensional fractal dimensions using the two-dimensional properties of fractal aggregates. Adv Colloid Interface Sci. 2004;112(1–3):49–57.
48. Kendall K, Kosseva MR. Nanoparticle aggregation influenced by magnetic fields. Colloids Surf Physicochem Eng Aspects. 2006;286(1–3):112–6.